AN INTEGRATED SELF-SENSING APPROACH FOR ACTIVE MAGNETIC BEARINGS

E. O. Ranft*, G. van Schoor and C. P. du Rand***

** School of Electrical, Electronic, & Computer Engineering, North-West University, Potchefstroom Campus, Private Bag X6001, Potchefstroom, 2520, South Africa E-mail: charl.durand@nwu.ac.za*
*** Unit for Energy Systems, North-West University, Potchefstroom Campus, Private Bag X6001, Potchefstroom, 2520, South Africa E-mail: george.vanschoor@nwu.ac.za*

Abstract: Self-sensing permits active magnetic bearings (AMBs) to consolidate the actuation and sensing functions into a single electromagnetic transducer. Eliminating the position sensing device as well as interfacing reduce potential system failure points, costs, and complexity. Self-sensing performance at present faces technical challenges such as magnetic cross-coupling, saturation, eddy currents, and system robustness. This work proposes an integrated self-sensing approach to collectively address mechanisms that contribute to modelling errors and position estimation inaccuracy. The self-sensing approach is based on the amplitude modulation technique and comprises a coupled reluctance network model (RNM) that is embedded in a nonlinear multiple input multiple output parameter estimator. The estimator employs a frequency-shifted model that is solved at a lower frequency to increase system performance. Furthermore, the RNM incorporates air gap fringing, complex permeability, and magnetic material nonlinearity terms. Magnetic saturation is accounted for using current scaling weights in the position estimation scheme. Basic functionality of the integrated self-sensing approach is demonstrated using an experimentally verified transient simulation model of the magnetic bearing. Verification and refinement of the RNM is accomplished through an iteration process using finite element method (FEM) results and experimental measurements. The simulation results show that the 40 node RNM can be accurate compared to an 80 000 node FEM analysis. Evaluation of the system stability margin indicates that the robustness of the magnetic bearing control is suitable for unrestricted long-term operation.

Keywords: Self-sensing, active magnetic bearing (AMB), electromagnetic actuator, coupled reluctance network, position estimation.

1. INTRODUCTION

Active magnetic bearings (AMBs) permit levitation of a rotor without mechanical contact at high rotational speeds, rendering them important components for modern industry. In the drive to promote wider industrial application, manufacturers and researchers aim to produce integrated AMB technology that is more reliable and economical. A self-sensing approach consolidates the actuation and sensing functions into a single electromagnetic transducer, thereby eliminating the position sensing device as well as the associated power, wiring, and interfacing. This directly reduces potential system failure points, cost, and complexity [1].

Although self-sensing offers a number of advantages over conventional displacement sensors, it remains a challenge [2]. Technical difficulties that limit self-sensing performance include eddy currents, magnetic material saturation, system robustness [2], and magnetic cross-coupling [3].

The literature describes different solutions to the magnetic saturation and cross-coupling problems. Skricka et al. [3] explores the application of a nonlinear magnetic reluctance model to reduce the effects of cross-coupling. Noh et al. [4] proposed a nonlinear parameter estimation technique to evaluate the effects of magnetic saturation. Maslen [2] states that switching ripple amplitude is fundamental for robust self-sensing AMBs. The resulting eddy currents can be mitigated by reducing the frequency of the excitation signal [2].

This work adopts the underlying theoretical principles of these individual techniques [2-4] to form the basis for an integrated self-sensing approach. The proposed self-sensing approach aims to collectively address the mechanisms that contribute to modelling errors and position estimation inaccuracy.

The solution is based on the amplitude modulation approach [5] and comprises a coupled reluctance network model (RNM) that is embedded in a nonlinear multiple input multiple output (MIMO) parameter estimator. The integrated approach implements a frequency-shifted model to reduce the computational complexity thereof. High frequency perturbations that arise from normal power amplifier (PA) switching is utilised to estimate the actuator inductance and hence, rotor displacement. Recent studies [5-8] concluded that the application of switching current ripple leads to increased robustness exceeding best achievable levels obtained by Morse et al. [9]. The accuracy of the magnetic circuit model is improved by incorporating air gap fringing, complex permeability, and magnetic material nonlinearity terms [10]. One of the difficult challenges facing self-sensing

researchers [11], magnetic saturation, is addressed using current scaling weights, which permits the actuator with the lowest flux density to contribute more to the position estimate. Furthermore, a first attempt to separate position estimation of the *x*-and *y*-axis using a single coupled RNM is also presented.

Verification and refinement of the RNM are accomplished through an iterative process using finite element method (FEM) results and experimental measurements. The performance limitations of the proposed self-sensing approach are investigated through simulations derived by a verified transient simulation model (TSM) of the experimental magnetic bearing.

2. MODELLING OF THE ACTUATOR

2.1 Governing equations

The self-sensing principle requires that the actuator can be described by a mathematical model. The quality of this model directly influences self-sensing performance. This work explores a RNM that models the fundamental frequency impedance of a heteropolar magnetic bearing with 8-poles. Figure 1 shows the referencing geometry of the AMB and rotor.

The poles of the magnetic bearing are magnetically coupled via leakage flux, rotor-iron, and stator back iron. The RNM topology is determined by the geometry of the specific experimental setup. Therefore, to model magnetic cross-coupling effects, a mutual leakage path is included between adjacent poles. Figure 2 shows one part of the corresponding reluctance model. The subscripts *p*, *r*, *s*, *l*, and *g* denote the pole, rotor, stator, leakage, and air gap respectively.

The governing equations are derived according to Skricka et al. [3]. If the network model consists of *P* poles, 5*P* linear independent equations link the magnetic bearing's 5*P* fluxes. The loop and flux conservation equations can be arranged in matrix form as

$$\mathbf{\Re \Phi = NI} \tag{1}$$

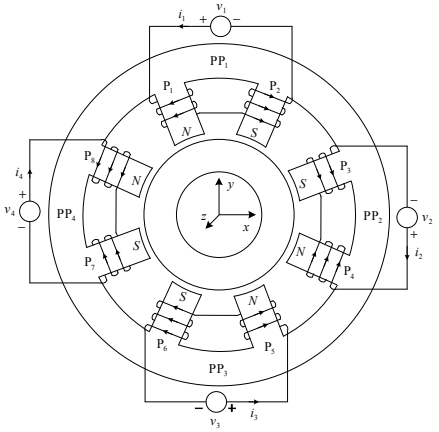

Figure 1: 8-pole heteropolar AMB with 4 coils [11].

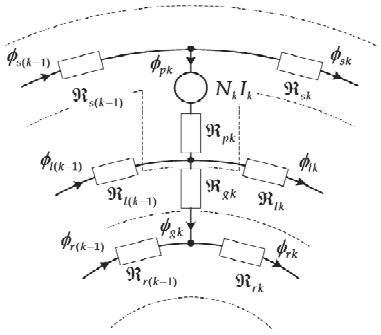

Figure 2: Mutual leakage reluctance network [3]

with the matrix $\mathbf{\Re}$ the reluctances, the vector $\mathbf{\Phi}$ the fluxes, the matrix **N** the number of coil windings, and the vector **I** the coil currents. The fluxes are determined by inverting the reluctance matrix. The inductances are obtained by [10]

$$\mathbf{L = T'\Re^{-1}N} \tag{2}$$

where the matrix **T** comprises 5*P* rows and *m* (number of coils) columns. The diagonal entries in the matrix denote the coil self-inductances and the off-diagonal entries the mutual inductances.

2.2 Reluctances

In Figure 2, $\Re_p$, $\Re_r$, and $\Re_s$, are obtained by

$$\Re = \frac{l}{\mu_0 \mu_r a_g} \tag{3}$$

where l is the effective magnetic material path length, μ_0 the permeability of free space, μ_r the magnetic material relative permeability (incorporates saturation and eddy current effects), and a_g the air gap area.

Conversely, the leakage reluctance $\Re_l$ (see Figure 2), which comprises the mutual leakage path reluctance $\Re_{lm}$ and the self-leakage path reluctance $\Re_{ls}$, is difficult to determine analytically. The leakage reluctance is therefore computed using genetic algorithm optimisation. A fitness function compares the RNM and a linear FEM analysis in terms of self-inductance, mutual inductances, and flux levels for each bearing coil.

The total magnetic path reluctance is mostly influenced by the air gap reluctance $\Re_g$. In this work, the influence of fringing, which denotes the flux spread at the air gap, is investigated. Fringing enlarges the effective air gap area, which reduces $\Re_g$. Since the fringing path for a radial AMB depends on various parameters as well as rotor position, determining $\Re_g$ analytically for varying rotor positions is difficult. Therefore, similar to $\Re_l$, $\Re_g$ is computed using a FEM analysis and genetic algorithm optimisation. Results generated by an analytical air gap model, which excludes fringing [3], and the FEM analysis, show large discrepancies. Therefore, to improve

the accuracy of the bearing model, fringing effects must be quantified.

2.3 Eddy currents

The coil current ripple due to PA switching and the resulting flux ripple, produces eddy currents, which reduce the flux carrying capacity of the magnetic material. A rate dependent material permeability term is used to model this effect [10]

$$\mu_{fd}(s)=\mu\left[\frac{\tanh\left(\sqrt{s\sigma\mu}\,\frac{d}{2}\right)}{\sqrt{s\sigma\mu}\,\frac{d}{2}}\right] \tag{4}$$

with $\mu = \mu_0\mu_r$ the material permeability, s the complex frequency, σ the electrical conductivity, and d the lamination thickness.

Equation (4) together with the incremental permeability are utilised to compute the complex material permeability. The switching frequency impedance results show that the correlation between experimental measurements and the RNM, determined by (2) and (4), is not satisfactory for self-sensing.

An alternative approach is explored in this work to account for eddy current effects. The complex material permeability, which is a function of flux density, is computed experimentally. A number of toroidal discs of the lamination material are stacked and excited with a switching PA through a primary coil. The switching frequency as well as flux density excursion used in the experimental magnetic bearing are employed in the setup. This approach showed marked improvement in correlation between measured and modelled results.

2.4 Magnetic material nonlinearity

To account for the nonlinear behaviour of the magnetic material, the model includes the flux density dependent relative permeability $\mu_r(B)$. The governing equations can be written in matrix form

$$\mathbf{\Re(\Phi)\Phi=NI}. \tag{5}$$

The curve of the nonlinear relative permeability is obtained from the peak magnetisation curve supplied by the manufacturer of the magnetic material.

2.5 Bearing model flow diagram

A flow diagram of the nonlinear RNM is presented in Figure 3. The model inputs are the (x, y) rotor position and the average coil currents (I_1 to I_4). The (x, y) coordinate is then utilised to obtain the reluctance values for each air gap. The fluxes in each section of the RNM are computed using the air gap reluctances, average coil currents, and initial material reluctances. Next, new values are determined for the material permeability ($\mu_0\mu_r$) in each section of the RNM. An iterative process is followed until a minimum is reached.

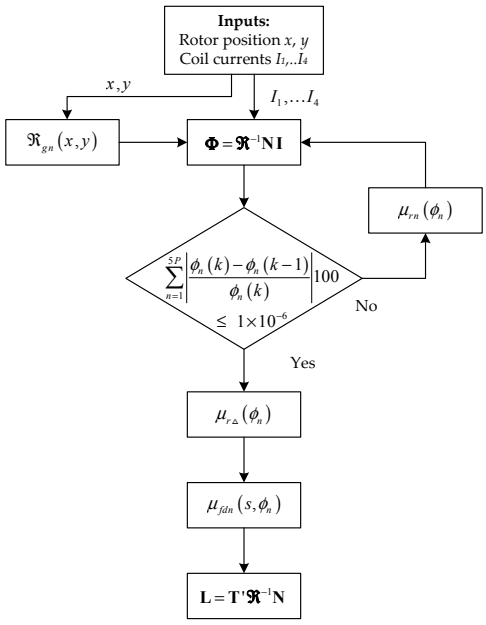

Figure 3: Nonlinear RNM flow diagram

The fluxes are used to compute the complex material permeability (μ_{fd}) for each section of the RNM. The complex inductance matrix is then utilised to determine the complex impedance given by $\mathbf{Z} = j\omega_s\mathbf{L}$ with ω_s the switching frequency.

The procedure followed to realise a refined model is:

- Construct FEM and initial RNM models using experimental bearing parameters.
- Identify and quantify problematic mechanisms that cause poor correlation. Repeat process until correspondence is satisfactory.
- Steady state validation: compare RNM with experimental RLC measurements and refine bearing parameters.
- Include switching frequency effects in RNM (fundamental frequency model).
- Dynamic validation: compare RNM with experimental results. Identify and quantify any discrepancies.

2.6 RNM verification

The RNM model is compared with FEM analyses. Table 1 documents the maximum absolute percentage errors between the RNM results and FEM analyses. Important results for the linear and nonlinear (includes magnetic material properties and I_1 = 6 A) cases are shown in Figures 4 and 5 respectively. In the figures, L_{jk}

Table 1: Summary of the modelling errors between the FEM and RNM results

Parameter	Maximum absolute error (%)		
	Linear	I_1= 2 A	I_1= 6 A
L_{11}	0.95	1.6	1.8
ϕ_1	0.85	0.8	0.3
ϕ_2	0.85	0.4	0.2
L_{12}	3.5	4.8	3.8
ϕ_3	11	3.5	8.8
ϕ_4	8	5	7.2

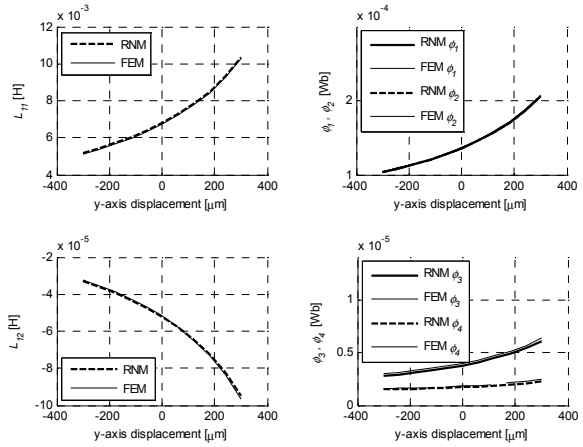

Figure 4: Linear mutual leakage RNM verification

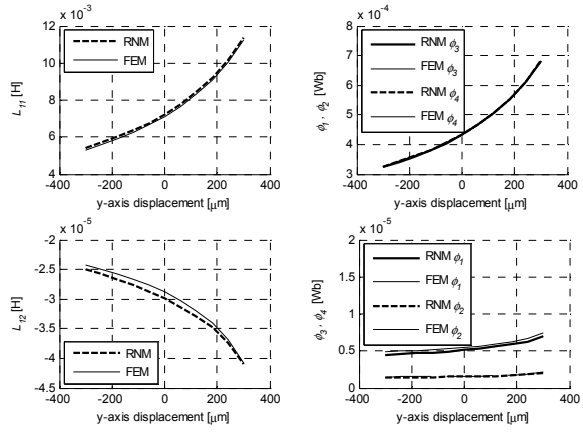

Figure 5: Nonlinear mutual leakage RNM verification

denotes the mutual inductance between the *j*-th and *k*-th coils, and ϕ_j signifies the magnetic flux in pole *j*.

The linear and nonlinear results presented show good correlation for different current levels. Discrepancies between the graphs are mainly attributed to measurement imprecision. The results show that the 40 node RNM can be accurate compared to an 80 000 node FEM analysis.

The AMB's coil impedance is determined at the switching frequency by exciting the coil of pole pair 1 (PP_1) with a switching PA. The coil currents and voltages are captured, after which a fast Fourier transform (FFT) is performed. The impedance is determined by dividing the fundamental voltage component by the corresponding current component. The improvement in absolute percentage errors between the modelled and measured results when using the experimental complex permeability in the RNM, for I_1 = 9 A, is 38 %, 35 %, and 48 % for Z_{11}, R_{e11}, and L_{11} respectively. The smaller errors show that the experimentally determined complex permeability remarkably improves model accuracy.

3. POSITION ESTIMATION SCHEME

3.1 Basic approach

The simulated position estimation scheme is shown in Figure 6. The proposed self-sensing approach is evaluated using a TSM of the experimental AMB. The TSM developed in [12] is adopted for this purpose and accurately models magnetic saturation, hysteresis, eddy currents, and cross-coupling effects.

The amplitude and phase of the fundamental current and voltage components are extracted. The RNM utilises the average coil currents to determine the flux distribution in the model. The switching frequency impedance is computed via the inductance matrix and used together with the complex voltages to determine the complex coil currents. The current errors are fed to PI controllers, which yield *x* and y rotor position estimates.

Each PP is treated as an isolated actuator to simplify the parameter estimator analysis. The information regarding rotor displacement is embedded in the inductance of the electromagnetic transducer. The relationship between the voltage, current, and position is given by [2, 11]

$$v=\mu_0 N^2 a\left[\frac{1}{2(g_0-x)+l/\mu_r}\frac{di}{dt}+2\frac{i}{\left(2(g_0-x)+l/\mu_r\right)^2}\frac{dx}{dt}\right]+iR \tag{6}$$

with *N* the number of coil turns, *a* the air gap area, g_0 the nominal air gap length, *x* the position of the suspended body, *l* the effective magnetic material path length, μ_r the magnetic material relative permeability, *i* the coil current, and *R* the coil resistance.

Equation (6) neglects leakage, fringing, and eddy-current effects, and assumes a uniform distribution of flux in the core and the air gap. Since the rotor position is assumed constant at the switching frequency, the *dx*/*dt* term is neglected. Furthermore, it is assumed that the coil resistance is small compared to the coil reactance at the switching frequency and that amplitude and phase extraction is ideal. Applying the Laplace transform to (6), expressing it in phasor form at the switching frequency ω_s, and neglecting core reluctance, produces the demodulated current estimate

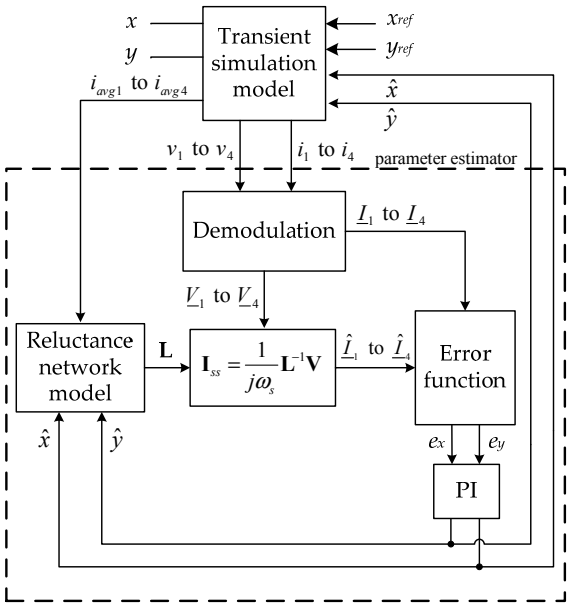

Figure 6: Position estimation scheme

$$\hat{\underline{I}} = \frac{1}{j\omega_s}\frac{2(g_0 \pm \hat{x})}{\mu_0 N^2 a}\underline{V}. \quad (7)$$

For a single degree of freedom, the amplitudes of the actual and estimated demodulated currents are compared and the error used to update the position estimate $\hat{x}$. This can be written as

$$x^* = \arg\min_{\hat{x}}\left(|\underline{I}| - |\hat{\underline{I}}(\hat{x})|\right) \quad \text{with} \quad \hat{x} \in [x_{min}, x_{max}] \quad (8)$$

where x_{min} and x_{max} are determined by the clearance of the backup bearing.

Figure 7 shows the position estimator for a single degree of freedom. The bearing coils are configured in differential mode and the top and bottom air gaps are given by (g_0 - x) and (g_0 + x) respectively. Linearity and signal to noise ratio of the estimated position signal are improved by using information from both coil currents.

The demodulated current amplitudes are subtracted from each other (opposing actuators), thereby eliminating the effect of the nominal air gap g_0 to produce the signal u. Since u is not only a function of rotor position, the voltage signals are demodulated and fed to a frequency shifted model, which yields demodulated current amplitude estimates. Next, $\hat{u}$ is subtracted from u to produce an error e. The error serves as input to the PI controller, which determines an estimate of the position $\hat{x}$. The estimate is adjusted until the difference in true and estimated demodulated coil currents are the same. The average currents are fed to the respective models to incorporate the working point dependency of the model. The demodulated current scaling weights λ are discussed in Section 4.

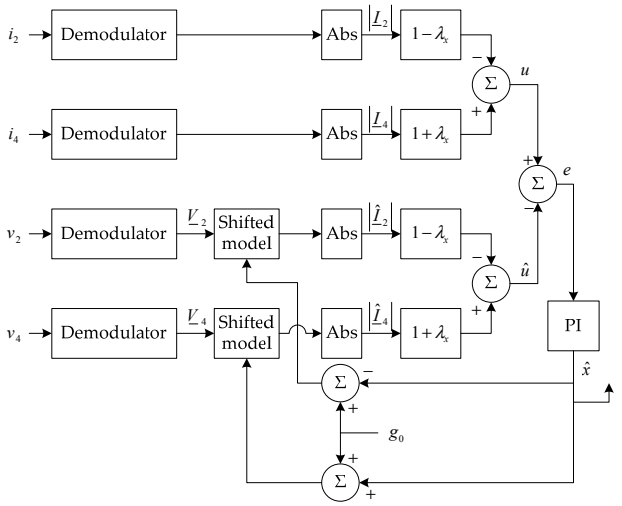

Figure 7: Position estimator schematic for a single degree of freedom (x-axis)

3.2 Demodulation process

Demodulation involves selecting a sample data window, removing any linear trends in the estimated spectrum, and performing an FFT to extract information regarding the fundamental components. Important variables that influence the FFT are window size and sampling rate [13]. Window size must be selected so that the switching frequency component exactly corresponds with one of the regularly spaced harmonic amplitude and phase components. Since the FFT's sampling rate is synchronised with PA switching, no aliasing filters are required in simulation. The transfer function of the demodulator is modelled using a sampler and zero-order hold circuit. It also comprises a second sampler and zero-order hold since the FFT is computed at a fixed rate. The transfer function of the demodulator is

$$F(s) = \frac{1}{T_1}\left(\frac{1-e^{-T_1 s}}{s}\right)\frac{1}{T_2}\left(\frac{1-e^{-T_2 s}}{s}\right) \quad (9)$$

where T_1 and T_2 denote the width of the sample window and the period of the FFT respectively.

The duty cycle plays an important role in the demodulation process since the amplitude and phase information of the first harmonic is a function thereof. The duty cycle is limited between $0.25 \leq \alpha \leq 0.75$ to ensure that the fundamental amplitude does not decrease below $1/\sqrt{2}$ of the maximum amplitude of $4V_p/\pi$. The ripple amplitude therefore never reduces to zero, increasing system robustness.

3.3 Parameter estimator stability

The relationship between demodulated current and duty cycle is established to facilitate a simplified block diagram of the parameter estimator. The output of the demodulator is related to the estimated position $\hat{x}$ using a

constant K, and is obtained via (7) and the fundamental amplitude of the voltage.

$$|\hat{\underline{I}}| = \frac{1}{\omega_s}\frac{2(g_0 \pm \hat{x})}{\mu_0 N^2 a}\frac{4V_p}{\pi}\sin(\pi\alpha) = K(g_0 \pm \hat{x}) \quad (10)$$

The effect of the duty cycle is modelled as a nonlinear time-varying gain that satisfies $K_{min} \leq K \leq K_{max}$. Combining (9) and (10), and assuming $K_2 = K_4 = K$, the error in Figure 7 is given by (11).

$$E = U - \hat{U} = 2KF(s)(X - \hat{X}) \quad (11)$$

Stability analysis is conducted using the circle criterion. This measure is sufficient to establish asymptotic stability for nonlinear time-variable systems, whose linear portion is not necessarily open-loop stable [14].

Since K is time-variable, a closed disk $D(K_{min}, K_{max})$ is defined in the complex plane symmetrical about the real axis. The circle criterion states that absolute system stability is guaranteed if the Nyquist plot of $2F(s)G(s)$, with $G(s)$ the PI controller transfer function, does not enter nor encircle disk D. This implies that the system is globally uniformly asymptotically stable for $K_{min} \leq K \leq K_{max}$ with arbitrary nonzero initial conditions. The circle incorporates all gain variations and is therefore a conservative measure for system stability. Figure 8 shows the circle criterion with disk D and the $2G(j\omega)F(j\omega)$-locus.

4. EVALUATION OF THE SENSOR

The experimental AMB on which the TSM is based is shown in Figure 9. The AMB system comprises two laminated heteropolar magnetic bearings, eddy-current position sensors, a 500 mm flexible rotor, independent 3 kVA (300 V, 10 A) current controlled switch-mode PAs, and a digital real-time controller. Important parameters are: PA switching frequency 20 kHz, nominal air gap 0.6 mm, rotor weight 7.7 kg, and magnetic material saturation flux density ±1.3 T.

The correspondence between the TSM and a measured 50 µm step response of the experimental AMB is shown

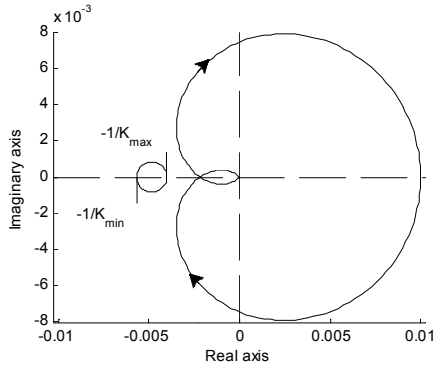

Figure 8: Estimator stability using the circle criterion

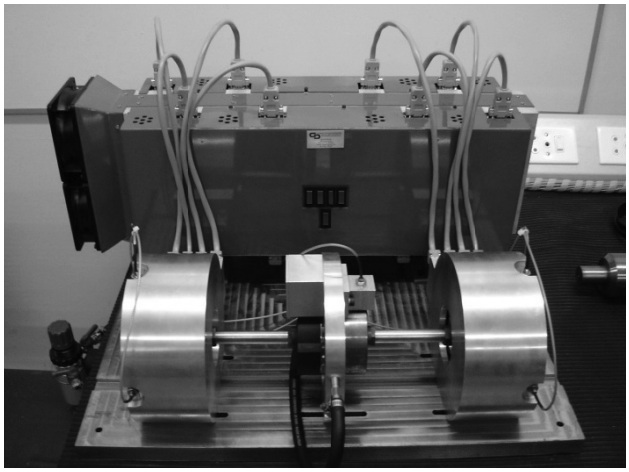

Figure 9: The experimental double heteropolar AMB

in Figure 10. The graph shows good correlation regarding signal rise time and percentage overshoot. The modelling inaccuracy is satisfactory for evaluating the proposed self-sensing application.

4.1 Magnetic cross-coupling

The influence of cross-coupling between the x-and y-axis is evaluated by suspending the rotor with the estimated position, and applying a 20 Hz sinusoidal disturbance force of 50 N in the x-axis. Figure 11 shows the simulation results where mutual inductance terms are included in the position estimation model.

The experiment showed that the system becomes unstable and that the rotor delevitates in the x-axis if mutual inductance terms are not included in the model. Figure 11 demonstrates that the proposed self-sensing sensor permits stable suspension of the rotor when the mutual inductance terms, which couples the different PPs, are included in the position estimation model. Furthermore, a marked improvement was noted in the y-axis displacement. The errors in the graphs are due to cross-coupling effects caused by the varying duty cycle.

4.2 Magnetic saturation

In order to quantify the effects of magnetic saturation on the integrated self-sensing approach, the magnetic bearing is driven intentionally into saturation. This is achieved by fixing the rotor in the zero x, y position, and applying the following current references:

- $i_{1ref} = i_{3ref} = 7.5$ A;
- $i_{2ref} = 7.5 + 7.5\sin(2\pi 10t)$; and
- $i_{4ref} = 7.5 - 7.5\sin(2\pi 10t)$.

This produces magnetic flux densities in excess of 1.3 T.

If one of the opposing PPs is driven into saturation, the slope of the inductance as function of position reverses, causing positive feedback. This will result in clamping of

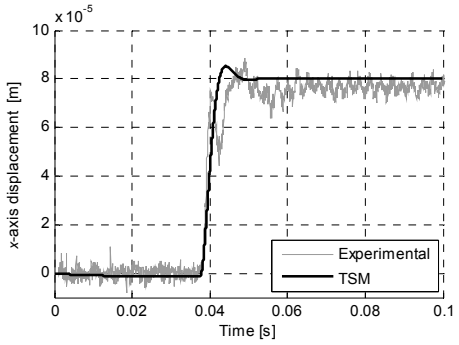

Figure 10: Measured and simulated AMB step response

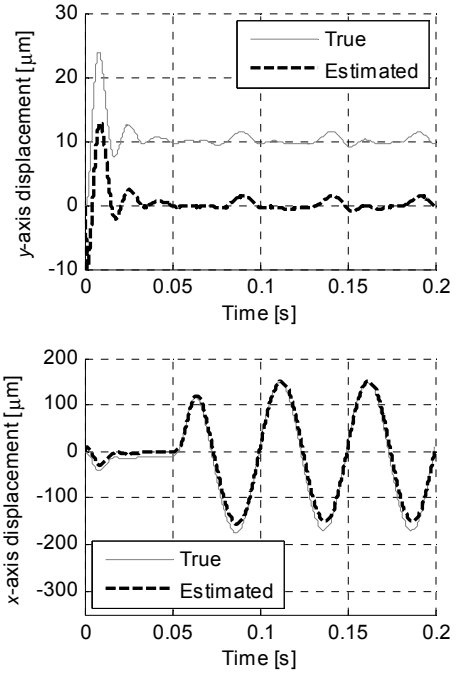

Figure 11: Dynamic cross-coupling effects

the rotor at the backup bearing limit. Following magnetic saturation, the actuator's inductance decreases, thereby increasing the current ripple. The signal of the saturated actuator therefore becomes more influential in the estimation of the position.

Magnetic saturation is accounted for by applying weights λ to scale the demodulated coil currents. The scaling factors ensure that the actuator with the lowest flux density contributes most to the estimate of the position. Using a scaled combination of both opposing demodulated coil currents instead of only the demodulated current of the PP with the lowest flux density, holds distinct advantages:

- Discontinuities are eliminated in the estimated position (occurs when switching between demodulated currents).
- Increased sensitivity and linearity with the differential PP configuration under normal operation.

The saturation factors λ_x and λ_y are obtained from (12)

$$\lambda_y = \left((B_1 - B_2) - (B_5 - B_6)\right)/2 \quad \{\lambda_y \in \mathbb{R} \mid -1 \le \lambda_y \le 1\}$$
$$\lambda_x = \left((B_4 - B_3) - (B_8 - B_7)\right)/2 \quad \{\lambda_x \in \mathbb{R} \mid -1 \le \lambda_x \le 1\} \tag{12}$$

where B_1 to B_8 denote the flux densities of poles P_1 to P_8 respectively.

Figure 12 shows the results of the magnetic saturation simulations. The position estimates show a small deviation from the dc offset for high flux densities. This result demonstrates that the integrated self-sensing approach can produce accurate position estimates for magnetically saturated conditions.

4.3 Stability margin

The negative stiffness of magnetic bearings due to static magnetic forces renders them inherently unstable [15]. Therefore, feedback control provides positive stiffness and damping to centre the rotor. The stability margin is an importance measure and signifies the robustness of the AMB control for variations in system parameters. In this work, the stability margin is evaluated according to ISO 14839-3 using the sensitivity function [15].

An excitation signal with varying frequency is applied to the magnetic bearing after the rotor is suspended with the true and estimated positions respectively. Figure 13 shows the Bode plots of the sensitivity functions. The figure shows that peak sensitivities of less than 8 dB are recorded for position control with the true and estimated position. The AMB is therefore categorised in Zone A according to the ISO standard [15], indicating that the robustness of the magnetic bearing control is suitable for unrestricted long-term operation.

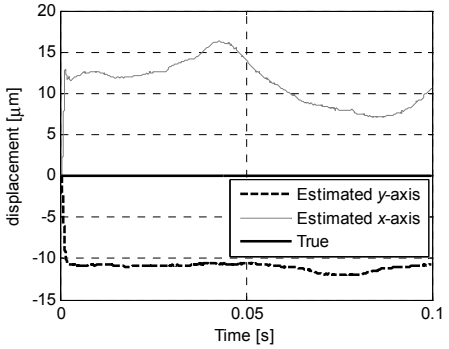

Figure 12: Effects of magnetic saturation

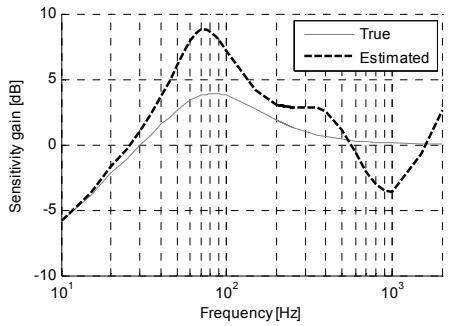

Figure 13: Bode plots of sensitivity functions

5. CONCLUSIONS

This paper explores an integrated self-sensing approach for AMB systems. The proposed solution collectively addresses, in part, problems associated with eddy currents, magnetic material saturation, system robustness, and magnetic cross-coupling.

The costs of manufacturing are reduced by incorporating mutual inductance terms in the bearing model to address magnetic cross-coupling effects without mechanical separation of the actuators. Magnetic saturation is accounted for by incorporating a term for the magnetic material nonlinearity, applying the RNM in a nonlinear parameter estimator, and scaling the demodulated coil currents to ensure that the actuator with the lowest flux density contributes most to the estimate of the position. The results indicate that the latter methodology allows stable suspension of the rotor for magnetically saturated conditions. A complex material permeability term is included using a lookup table to model the effects of eddy currents. Estimation of the air gap reluctance is improved by introducing an air gap fringing term. The results show that the 40 node RNM can be accurate compared to an 80 000 node FEM analysis. The fact that processing times of RNMs are less than similar FEM analyses renders them an attractive solution for real-time implementation.

The performance of the proposed self-sensing approach is evaluated via static and dynamic tests. Technical challenges that were addressed include magnetic cross-coupling, magnetic saturation, and stability margin. Evaluation of the system stability margin indicates that the robustness of the magnetic bearing control is suitable for unrestricted long-term operation. Since the focus of this work was to demonstrate the feasibility of an integrated self-sensing approach, optimisation of the position estimator is still required to further increase system robustness.

However, to date, commercially viable applications place only modest demands on the sensing system. In order to realise a self-sensing scheme that will meet more stringent requirements, future work is still needed to address several technical issues. Self-sensing technology therefore remains a tough challenge that should stimulate continued research.

6. REFERENCES

[1] B. Hanson and M. Levesley: "Self-sensing applications for electromagnetic actuators", *Sensors and Actuators A*, Vol. 116, pp. 345-351, June 2004.

[2] E.H. Maslen: "Self-sensing for active magnetic bearings: overview and status", *Proceedings: 10th International Symposium on Magnetic Bearings*, Switzerland, pp. 13-19, August 2006.

[3] N. Skricka and R. Markert: "Influence of cross-axis sensitivity and coordinate coupling on self-sensing", *Proceedings: 6th International Symposium on Magnetic Suspension Technology*, Italy, pp. 179-184, October 2001.

[4] M.D. Noh and E.H: "Maslen, Self-sensing magnetic bearings (Part I & II)", *Proceedings: 5th International Symposium on Magnetic Bearings*, Japan, pp. 95-100 & 113-118, August 1996.

[5] A. Schammass, R. Herzog, P. Bühler and H. Bleuler: "New results for self-sensing active magnetic bearings using modulation approach", *IEEE Transactions on Control Systems Technology*, Vol. 13 No. 4, pp. 509-516, July 2005.

[6] A. Schammass: *A self-sensing active magnetic bearing: Modulation approach*, PhD thesis, Swiss Federal Institute of Technology Lausanne - EPFL, Lausanne, Switzerland, July 2003.

[7] D.T. Montie: *Performance limitations and self-sensing magnetic bearings*, PhD thesis, University of Virginia, Virginia, USA, January 2003.

[8] E.H. Maslen, D.T. Montie and T. Iwasaki: "Robustness limitations in self-sensing magnetic bearings", *ASME Journal of Dynamic Systems, Measurement and Control*, Vol. 128, pp. 197-203, June 2006.

[9] N. Morse, R. Smith, B. Paden and J. Antaki: "Position sensed and self-sensing magnetic bearing configurations and associated robustness limitations", *Proceedings: 37th IEEE Conference on Decision and Control*, Vol. 3, pp. 2599-2604, December 1998.

[10] D.C. Meeker, E.H. Maslen and M.D. Noh: "An augmented circuit model for magnetic bearings including eddy currents, fringing, and leakage", *IEEE Transactions on Magnetics*, Vol. 32 No. 4, pp. 3219-3227, July 1996.

[11] G. Schweitzer and E. Maslen: *Magnetic Bearings: Theory, Design, and Application to Rotating Machinery*, Springer-Verlag, Berlin, Heidelberg, chapter 15, pp. 435-459, January 2009.

[12] M. D. Noh, D. T. Montie and E. H. Maslen: "A simulation model for the analysis of transient magnetic bearing performance", *Proceedings: 7th International Symposium on Magnetic Bearings*, Zurich, Switzerland, pp. 177-181, Aug. 2000.

[13] E. Ifeachor and B. Jervis: *Digital signal processing: A practical approach*, 2nd ed. Prearson Education, Harlow, England, chapter 11, pp. 681-725, 2002.

[14] S.M. Shinners, *Modern control system theory and application*, 2nd ed., Addison-Wesley Publishing Company, Massachusetts, chapter 1, 1978.

[15] ISO TC108/SC2/WG7 AMB: *Mechanical vibration: Vibration of rotating machinery equipped with active magnetic bearings - Part 3: Evaluation of stability margin*, ISO Standard 14839-3:2006, February 2007.